Finite element analysis of heat transfer by natural convection in porous media in vertical enclosures

Investigations in Darcy and non-Darcy regimes

Received March 1995
Revised April 1996

B.V.K. Satya Sai
School of Mechanical Engineering, Cranfield University, Bedford, UK
K.N. Seetharamu
Department of Mechanical Engineering, Indian Institute of Technology, Madras, India, and
P.A. Aswathanarayana
Department of Applied Mechanics, Indian Institute of Technology, Madras, India

Nomenclature

A = Aspect ratio $\left[\frac{H}{r_o - r_i}\right]$
c = Specific heat, J/kg – K
Da = Darcy number $\left[\frac{K}{L_{ref}^2}\right]$
$d\Gamma$ = Boundary of integration
$d\Omega$ = Volume of integration
g = Acceleration due to gravity, m/s^2
H = Height of the cavity, m
K = Permeability of porous medium, m^2
k = Thermal conductivity, $W/m - K$
k_m = Equivalent thermal conductivity of porous medium $[\Phi k_f + (1 - \Phi)k_s]$, $W/m - K$
L_{ref} = Reference length $[r_o - r_i]$, m
Nu = Local Nusselt number
$\overline{Nu}$ = Average Nusselt number
$\bar{P}$ = Pressure, N/m^2
P = Non-dimensional pressure $\left[\frac{\bar{P}L_{ref}^2}{\rho\alpha^2}\right]$
Pr = Prandtl number $\left[\frac{\nu}{\alpha}\right]$
q = Constant heat flux, W/m^2
Ra = Rayleigh number
$\left[\frac{L_{ref}^3 g\beta\Delta T}{\alpha\nu}\right]$ for constant wall temperature case
$\left[\frac{L_{ref}^4 g\beta q}{\alpha\nu k_m}\right]$ for constant wall heat flux case
$\overline{Ra}$ = Modified Rayleigh number (for constant wall ΔT case)
$\left[\frac{g\beta\Delta T L_{ref} K}{\nu\alpha}\right]$

The authors thank the National Science Foundation, USA for rendering the financial support (Grant No. INT-8903119) for carrying out this work.

International Journal for Numerical Methods for Heat & Fluid Flow
Vol. 7 No. 4, 1997, pp. 367-400.

Ra^* = Modified Rayleigh number (for constant q case) $\left[\frac{g\beta q L_{ref} K}{\nu\alpha k_m}\right]$

r = Radius of annulus, m

$\bar{T}$ = Temperature, K

U = Non-dimensional velocity

$\bar{U}$ = Velocity, m/s

X = Co-ordinate axis

Greek

α = Thermal diffusivity of porous medium $\left[\frac{k_m}{\rho c}\right], m^2/s$

β = Volumetric coefficient of expansion w.r.t. temperature, K^{-1}

ΔT = Reference temperature difference, K

Φ = Porosity of the matrix

κ = Radius ratio $\left[\frac{r_o}{r_i}\right]$

ν = Kinematic viscosity of fluid, m^2/s

ρ = Mass density, kg/m^3

σ = Coefficient in energy equation $\left[\frac{\Phi(\rho c)_f + (1-\Phi)(\rho c)_s}{(\rho c)_f}\right]$

τ = Non-dimensional time $\left[\frac{\bar{\tau} L_{ref}^2}{\alpha}\right]$

$\bar{\tau}$ = Time, s

Subscripts

1 = Vertical direction

2 = Horizontal direction

i = Inner wall

f = Fluid

o = Outer wall

s = Solid

Superscripts

* = Fictitious or pseudo (only in case of velocities)

n = Present time-step (nth time-step)

Introduction

Heat transfer by natural convection in a porous medium saturated with a fluid represents an area of rapid growth in contemporary heat transfer research. This has several important geophysical and engineering applications such as regenerative heat exchangers containing porous material, heat transfer through double walls filled with fibrous or granular insulation, heat transfer in grain storage installations, burying of drums containing heat generating chemicals in the earth, etc. Most of the significant analytical and numerical investigations carried out earlier on heat transfer in porous media[1-9] were based on the Darcy flow model, according to which the volume averaged velocity in a particular direction is proportional to the net pressure gradient in that direction. However, when permeability of the porous medium is high, Darcy law does not yield correct results and has to be modified modified appropriately. One such modification is the Brinkman extension, which accounts for the transition from Darcy flow to a highly viscous flow (without a porous matrix) in the limiting condition of extremely high permeability.

Chan *et al.*[10] were probably the first to use Brinkman extension to Darcy law. Their results show that for $Da < 10^{-3}$, the Brinkman extended equation and Darcy law give the same result. However, the range of Ra considered by them is too low (<300) to bring out the effect of permeability properly. Tong and Subramaniam[11] used modified the Oseen method to solve the boundary layer equations in a non-Darcy regime. They defined a parameter

$$E = \frac{\overline{Nu}\,Ra Da}{A}.$$

$E < 10^{-4}$ which fixes the limit for Darcy regime. A numerical verification of their results was later carried out by Lauriat and Prasad[12]. Sen[13] also included the convective terms in the equations but found that the effect is negligible. He showed that for an aspect ratio of 0.1, the Brinkman model and the Darcy flow model give virtually the same results when Da based on depth is less than 10^{-4}. Vasseur *et al.*[14] considered steady-state natural convection in a shallow porous cavity with uniform heating and cooling through opposite walls. Approximate solutions were obtained by assuming parallel flow in the core region and numerical solutions were obtained using the finite difference method. Da considered by them was 10^{-7} to 10^{-2} (based on depth) and Ra^* was $10 \leq Ra^* < 8 \times 10^4$ (based on depth). Aspect ratios of 0.33 and 0.25 (according to the present notation) were considered. They observed that, though $\overline{Nu}$ increases with Ra^*, it asymptotically reaches a constant value which depends on Da. They also stated that aspect ratio (A) is not a parameter of influence if it is less than 0.5. Vasseur *et al.*[15] also documented flow and heat transfer characteristics in an inclined porous medium with uniform heating and cooling through opposite sides. Again a shallow cavity ($A = 0.25$) was used. Thus, their analyses were basically confined to non-Darcy behaviour in shallow enclosures with uniform heating on the opposite walls.

Another modification is the addition of a Forchheimer term[16], which accounts for the non-linear drag as pore diameter increases. However, neither of these models adequately accounts for the transition from porous medium flow to a pure fluid flow as permeability of the medium increases. So a model which also takes into consideration the flow inertia terms serves this purpose. However, a somewhat recent study[17] shows that the inclusion of the inertia term is of no consequence and it only adds to the computational cost. However, it is preferable to retain this term when the model is intended to bridge the entire domain between low and high permeabilities. In the literature one comes across a model that includes not only the inertia terms but also both the Brinkman and Forchheimer extensions[18,19]. However, the validity of such a formulation has been questioned by Nield and Bejan[20]. In order for the Brinkman equations to be valid, the porosity must be high, and there is some uncertainty about the validity of Forchheimer's law at large porosities. So in the present study, a model that contains the inertia terms and the Brinkman extension along with the Darcy resistance term has been adopted for the numerical investigation into both Darcy and non-Darcy regimes.

In the area of numerical methods there has, of late, been an increase of interest in finite element schemes based on operator splitting methods. So in the present work, attention is also focused on one such operator splitting scheme, which renders itself to an efficient finite element code for the study of natural convection heat transfer in porous media. Successful use of a semi-implicit

operator-splitting scheme has been reported in Ramaswamy *et al.*[21] and Satya Sai[22] for convection problems in pure fluids (i.e. without a porous matrix). This scheme has been extended in the present study to porous media. This essential1y requires the incorporation of the Darcy resistance term as an additional source term in the conservation equations for momenta.

In the following section, we present the governing equations for natural convection heat transfer in porous media in axisymmetric geometries and numerical methodology. This is followed by the results and discussion section. In the first part of the results and discussion, we present the application of this scheme to the Darcy regime. Two types of geometries, viz. annular cavities and rectangular cavities are considered with a fairly wide range of parameters. Also, two types of boundary conditions are considered. The first of these deals with a cavity with isothermal vertical walls, while the horizontal walls are adiabatic. The second deals with a cavity, one of the vertical walls of which is supplied with a uniform heat flux while the other vertical wall is maintained at a uniform temperature. The only reports which deal with the above two types of boundary conditions in a very extensive manner are [7] and [8]. However, these analyses were based on the Darcy flow model. So the results of this subsection not only validate the present general model in the Darcy regime but also discuss some important aspects of velocity and thermal fields. In addition, correlations for the heat transfer coefficient for a wide range of parameters for the above two geometries and boundary conditions are presented. The second part of the results and discussion section deals with the non-Darcy regime, where the high permeability of the porous medium results in significant differences in flow and thermal fields as compared to the low permeability regime. Two different boundary conditions are considered. However, the analyses of this part are confined to plane cavities. This work is motivated by the absence of any study documenting the effect of permeability on flow and thermal fields in a fluid saturated porous medium in rectangular enclosures.

Governing equations and solution methodology

Considering X_1 axis to represent the vertical direction and X_2, the horizontal direction, the non-dimensional equations for natural convection in a fluid saturated porous medium in axisymmetric geometries can be written as follows.

The continuity equation:

$$\frac{\partial U_1}{\partial X_1} + \frac{1}{X_2}\frac{\partial}{\partial X_2}[X_2 U_2] = 0 \tag{1}$$

Momentum equation:

$$\frac{\partial U_1}{\partial \tau} + U_1\frac{\partial U_1}{\partial X_1} + U_2\frac{\partial U_1}{\partial X_2} = -\frac{\partial P}{\partial X_1} - \frac{Pr}{Da}U_1 + Pr\left[\frac{1}{X_2}\frac{\partial}{\partial X_2}\left(X_2\frac{\partial U_1}{\partial X_2}\right) + \frac{\partial^2 U_1}{\partial X_1^2}\right] + RaPrT \tag{2}$$

X_2 momentum equation:

$$\frac{\partial U_2}{\partial \tau} + U_1 \frac{\partial U_2}{\partial X_1} + U_2 \frac{\partial U_2}{\partial X_2} = -\frac{\partial P}{\partial X_2} - \frac{Pr}{Da} U_2 + Pr \left[\frac{1}{X_2} \frac{\partial}{\partial X_2} \left(X_2 \frac{\partial U_2}{\partial X_2} \right) + \frac{\partial^2 U_2}{\partial X_1^2} - \frac{U_2}{X_2^2} \right] \quad (3)$$

Energy equation:

$$\sigma \frac{\partial T}{\partial \tau} + U_1 \frac{\partial T}{\partial X_1} + U_2 \frac{\partial T}{\partial X_2} = \left[\frac{1}{X_2} \frac{\partial}{\partial X_2} \left(X_2 \frac{\partial T}{\partial X_2} \right) + \frac{\partial^2 T}{\partial X_1^2} \right] \quad (4)$$

Here all the lengths are non-dimensionalized using an L_{ref}, all the velocities by using $\frac{\alpha}{L_{ref}}$, pressure by using $\frac{\rho \alpha^2}{L_{ref}^2}$ and time by $\frac{\alpha}{L_{ref}^2}$.

Temperatures are non-dimensionalized according to the problem considered. The following assumptions are employed while using the above equations:

(1) Fluid properties are constant, except for the density variations in producing the buoyancy force.

(2) Dispersion effects and channelling effects are neglected in the porous medium.

(3) Fluid and porous media are combined and treated as a homogeneous medium.

(3) Effective thermal conductivity (k_m) of the solid-fluid mixture is measured for the combination.

(5) Porous medium is assumed to be isotropic.

(6) Brinkman viscosity is assumed to be same as fluid viscosity for convenience (but in general they are only approximately equal).

The numerical scheme is based on a semi-implicit operator splitting (or time-stepping) algorithm and is similar in structure to Chorin's[23] projection scheme which was originally developed in a finite difference context for solving the time-dependent Navier-Stokes equations. Briefly, the solution is advanced in four stages at each time-step. They are:

(1) calculation of fictitious (or pseudo) velocities from the momenta equations by dropping the pressure terms;

(2) evaluation of pressure from a pressure Poisson equation;

(3) correction of pseudo velocities to obtain velocities at the next time-step; and

(4) finally, calculation of temperature field from the velocity field obtained above.

One significant aspect of the present scheme is that a second order Adams-Bashforth scheme is used for advection terms, while the diffusion terms are treated in an implicit manner. Various advantages of the present scheme, *vis-à-vis* the explicit scheme, have been discussed in [21] and [22] for forced

convection problems in pure fluids and for natural convection problems in pure fluids, respectively. Galerkin finite element technique with linear triangular elements for domain discretization has been used to arrive at the following algebraic equations.

Fictitious velocity step:

$$\left[M + \left(K^{U_1}\right)\right] U_1^* = MU_1^n + \Delta\tau^n \left[F^{U_1} - AU_1^n + GT^n + QU_1^n\right] \tag{5}$$

$$\left[M + \left(K^{U_2}\right)\right] U_2^* = MU_2^n + \Delta\tau^n \left[F^{U_2} - AU_2^n + QU_2^n\right] \tag{6}$$

Pressure Poisson equation:

$$\left[K^P\right] P^{n+1} = F^P \tag{7}$$

Velocity correction:

$$M_D {U_1}^{n+1} = M_D U_1^* + \Delta\tau^n R^{U_1} \tag{8}$$

$$M_D {U_2}^{n+1} = M_D U_2^* + \Delta\tau^n R^{U_2} \tag{9}$$

Temperature calculation:

$$\left[M + \left(K^T\right)\right] T^{n+1} = MT^n + \Delta\tau^n \left[F^T - AT^n\right] \tag{10}$$

Various terms in the above equations are:

$$M_{ij} = \int_\Omega N_i N_j d\Omega$$

$$A_{ij} = \frac{3}{2}\int_\Omega N_i \left[N_k (U_1^n)_k \frac{\partial N_j}{\partial X_2} + N_k (U_2^n)_k \frac{\partial N_j}{\partial X_1}\right] d\Omega - \frac{1}{2}\int_\Omega N_i \left[N_k \left(U_1^{n-1}\right)_k \frac{\partial N_j}{\partial X_2} + N_k \left(U_2^{n-1}\right)_k \frac{\partial N_j}{\partial X_1}\right] d\Omega$$

$$K_{ij}^P = \int_\Omega \left[\frac{\partial N_i}{\partial X_1}\frac{\partial N_j}{\partial X_1} + \frac{\partial N_i}{\partial X_2}\frac{\partial N_j}{\partial X_2}\right] d\Omega\,; \quad K_{ij}^T = K_{ij}^P\,; \quad K_{ij}^{U_1} = Pr\, K_{ij}^P$$

$$K_{ij}^{U_2} = \int_\Omega Pr \left[\frac{\partial N_i}{\partial X_1}\frac{\partial N_j}{\partial X_1} + \frac{\partial N_i}{\partial X_2}\frac{\partial N_j}{\partial X_2} - \frac{N_i N_j}{{X_2}^2}\right] d\Omega$$

$$G_{ij} = RaPrM_{ij}\,; \quad Q_{ij} = -\frac{Pr}{Da} M_{ij}$$

$$F_i^{U_1} = \int_\Gamma N_i \frac{\partial U_1}{\partial \eta} d\Gamma ; \quad F_i^{U_2} = \int_\Gamma N_i \frac{\partial U_2}{\partial \eta} d\Gamma$$

$$F_i^P = \int_\Gamma N_i \frac{\partial P}{\partial \eta} d\Gamma - \frac{1}{\Delta \tau^n} \left[\int_\Omega \left[\frac{\partial N_k}{\partial x_1} (U_1^*)_k + \frac{\partial N_k}{\partial x_2} (U_2^*)_k \right] \right] d\Omega + \int_\Omega \frac{N_i N_k}{X_2} (U_2^*)_k \, d\Omega$$

$$F_i^T = \int_\Gamma N_i \frac{\partial T}{\partial \eta} d\Gamma$$

$$R_i^{U_1} = \int_\Omega N_i \frac{\partial N_k}{\partial X_1} P_k^{n+1} d\Omega ; \quad R_i^{U_2} = \int_\Omega N_i \frac{\partial N_k}{\partial X_2} P_k^{n+1} d\Omega$$

Here $d\Omega = 2\pi X_2 \, dX_1 \, dX_2$; Ω and Γ denote integration over the computational domain (Ω) and the boundary (Γ) respectively; η denotes the outward drawn normal to the boundary; N_i, N_j, etc., refer to the shape functions associated with nodes i, j, etc. respectively; summation over various nodes is implied on the repeated index k(k = 1 to 3); a superscript U_1, U_2, P or T refers to matrices associated with U_1, U_2, P or T respectively; M_D is the diagonalized mass matrix; A is the advection matrix; K^{U1}, K^{U2}, K^T are diffusion matrices; K^P is the pressure stiffness matrix; F^{U1}, F^{U2}, F^P, R^{U1} and R^{U2} are matrices on the right side of equations; G refers to the buoyancy term and Q refers to the Darcy resistance term.

Results and discussion

Investigations in the Darcy regime

A non-uniform, graded mesh of size 39×39 nodes with linear triangular elements has been used for all the cases considered. The mesh has been found to be adequate for the present work on the basis of a preliminary study on grid convergence. The details of this study are not presented here. Also in this part of the paper a Darcy number (Da) of 5×10^{-7} has been used, so that the investigations lie in the Darcy regime (or low permeability regime). The results, with appropriate boundary conditions, are presented in the subsequent sub-sections.

Uniform wall temperature cases. Figure 1 shows the geometry and boundary conditions for this case. The figure represents an axisymmetric annulus of inner radius r_i and outer radius r_0. The inner (hot) wall is maintained at a uniform temperature $\overline{T}_i$, while the outer(cold) wall is maintained at temperature $\overline{T}_0$. The two horizontal walls are assumed to be insulated. The same geometry represents a rectangular cavity for very large values of r_i and r_0. In this case the radius ratio nearly becomes equal to 1. Temperature non-dimensionalization is done as

$$T = \frac{\overline{T} - \overline{T_o}}{\Delta T} \quad \text{where} \quad \Delta T = \overline{T_i} - \overline{T_o} \tag{11}$$

As indicated earlier, the only exhaustive study of this geometry was made in [8] on the basis of Darcy law. So it is proposed to carry out a similar study with the

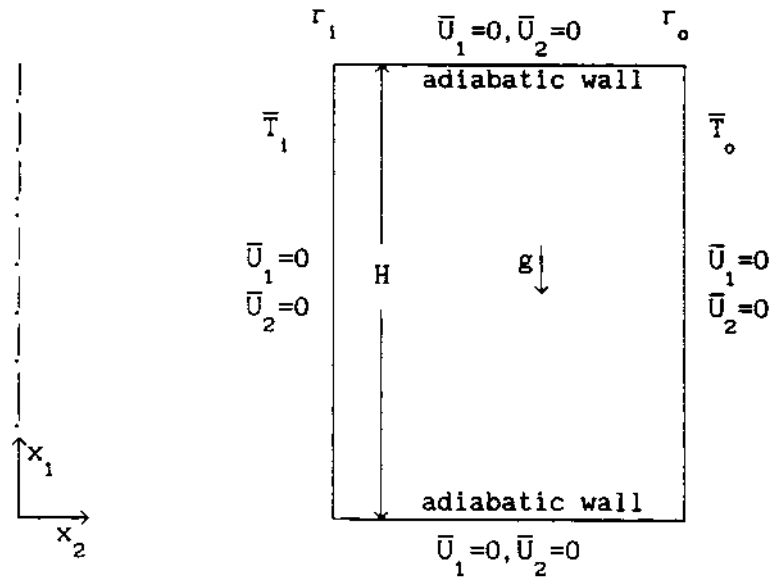

Figure 1.
Geometry and boundary conditions for constant wall temperature problem

present model for a wide range of aspect ratios (A) and radius ratios (κ). The range of parameters investigated is given below:

- aspect ratio (A) : 1, 2, 5, 10;
- radius ratio (κ) : 1, 2, 11, 16;
- Darcy number (Da) : 5×10^{-7};
- modified Rayleigh number ($\overline{Ra}$) ($\overline{Ra} = RaDa$) : 100, 500, 1000, 2000, 5000.

Figure 2 shows the variation of the non-dimensional vertical component of velocity (U_1) along the horizontal mid-plane of a square cavity for different modified Rayleigh numbers ($\overline{Ra}$). While the no slip condition prevails on the wall, very near to the wall the U_1 velocity attains a peak and then drops to almost zero in the core of the medium. This is in contrast with natural convection in a cavity with a pure fluid, in which case, the velocity peak is seen slightly away from the wall. For a porous medium, as a result of strong conductive effects, the velocities are confined to a very narrow region near the wall. This figure also confirms the agreement between the present model and Darcy flow model for the low permeability regime. According to Darcy law, velocity slip is permitted on the wall and the velocity attains a peak on the wall itself. In Figure 2 also the velocity peak is seen very close to the wall. Figure 3 brings out the effect of aspect ratio (A) and radius ratio (κ) on U_1 along the same plane as considered earlier. As A increases, the velocity peak increases, though only slightly. But the symmetry of velocity profile observed for a plane cavity (Figure 2) is not seen in Figure 3. U_1 velocity near the hot wall would be much higher than near the cold wall. A similar effect was observed for natural

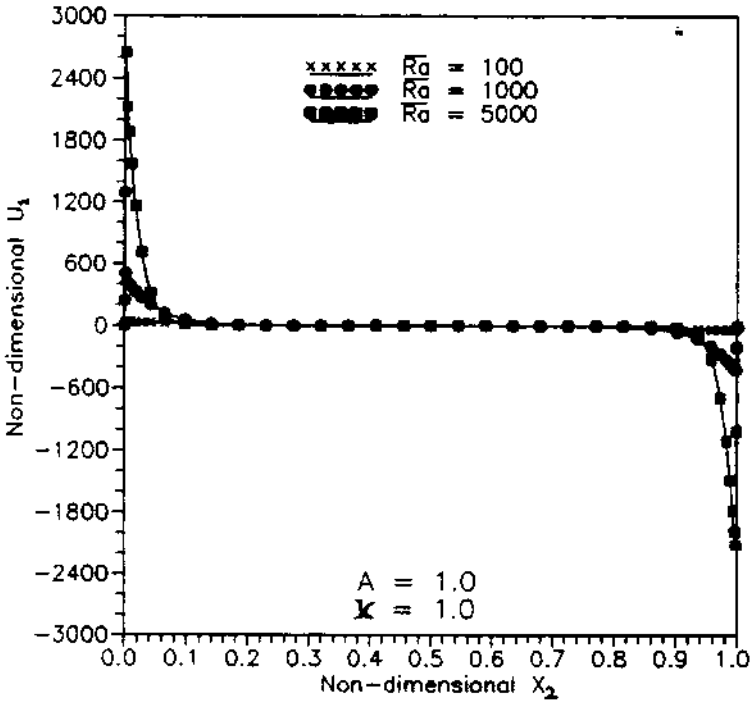

Figure 2.
Variation of vertical component of velocity along horizontal mid-plane of a square cavity for different modified Rayleigh numbers (A = 1, κ = 1)

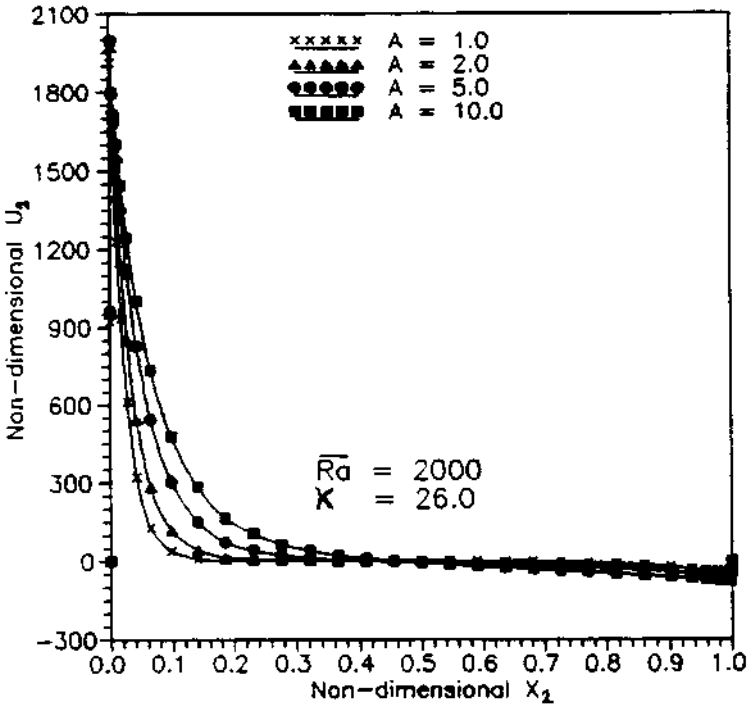

Figure 3.
Variation of vertical component of velocity along horizontal mid-plane of the annular cavity for different aspect ratios ($\overline{Ra}$ = 2,000, κ = 26)

convection in an annular enclosure filled with a pure fluid[22]. A stream of fluid which convects upwards along the hot wall descends along the cold wall. However, the area available near the hot wall is less than that near the cold wall. This results in an increase in velocity near the hot wall to preserve continuity. Figure 4 shows temperature contours along the horizontal mid-plane for different radius ratio (κ). In all these cases, A is taken as 1. The effect on temperature profiles is similar to that on a U_1 field. For a fixed κ, as $\overline{Ra}$ increases, the effect of convection becomes more and more predominant, resulting in thinner boundary layers near the hot wall. For $\kappa = 1$, which represents a plane cavity, the core of the porous medium is at the mean temperature and the temperature profiles are symmetric. However, as κ

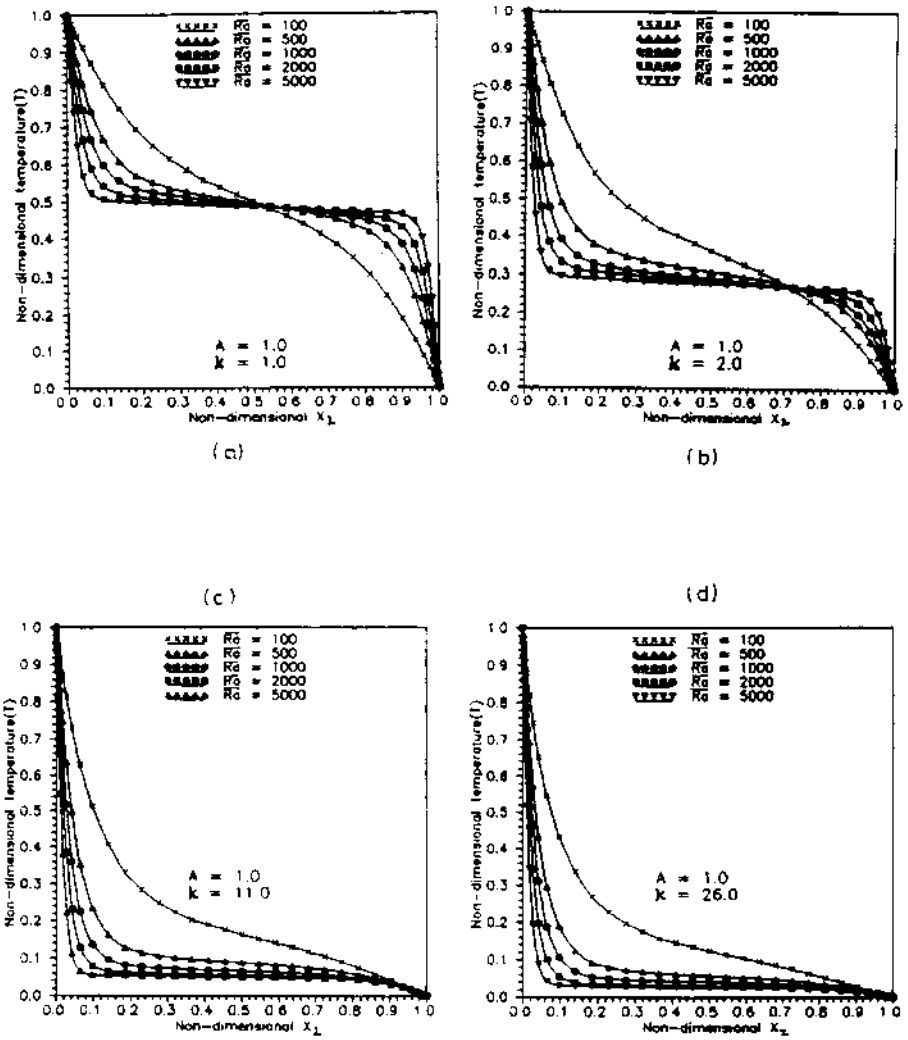

Figure 4.
Variation of temperature along horizontal mid-plane of the annular cavity of aspect ratio 1 for different Rayleigh numbers (a) $\kappa = 1$, (b) $\kappa = 2$, (c) $\kappa = 11$, (d) $\kappa = 26$

increases, the effect of curvature comes into picture. Once again, this effect is similar to that which has been observed for pure fluids[22]. Temperature drops down near the hot wall and the core temperature will be less than for a plane cavity. This drop in temperature increases with κ. Figure 5 shows the effect of A on the temperature plots for $\kappa = 1$. For higher A, the core width is seen to be smaller. This shows that conduction effects become predominant as A increases.

Figures 6 and 7 show the streamlines and isotherms for a square cavity ($A = 1$) with $\kappa = 1$ and 11 respectively. Similar observations as were made by earlier investigations based on Darcy law[8] could be made. For a fixed $\overline{Ra}$ as κ increases to 11, the flow field shifts to the upper right corner, the shift becoming more predominant at higher $\overline{Ra}$. It was observed in [8] that no multi-cellular flow is visible even at higher $\overline{Ra}$. However, in the present results, multi-cellular flow pattern is observed at $\overline{Ra} = 5{,}000$ for $\kappa = 1$; but the same is not observed as κ increases to 11. Also from the streamline pattern, we observe that for a particular κ as $\overline{Ra}$ increases, the orientation of the streamlines rotates in the clockwise direction. The greater boundary layer growth on the hot wall at higher $\overline{Ra}$ tends to rotate the core structure in the clockwise direction. Also from the isothermal patterns in Figures 6 and 7, we find that as κ increases for a given $\overline{Ra}$, the isotherms shift more towards the hot wall and, once again, this shift becomes more predominant at higher $\overline{Ra}$. This results in a destruction of

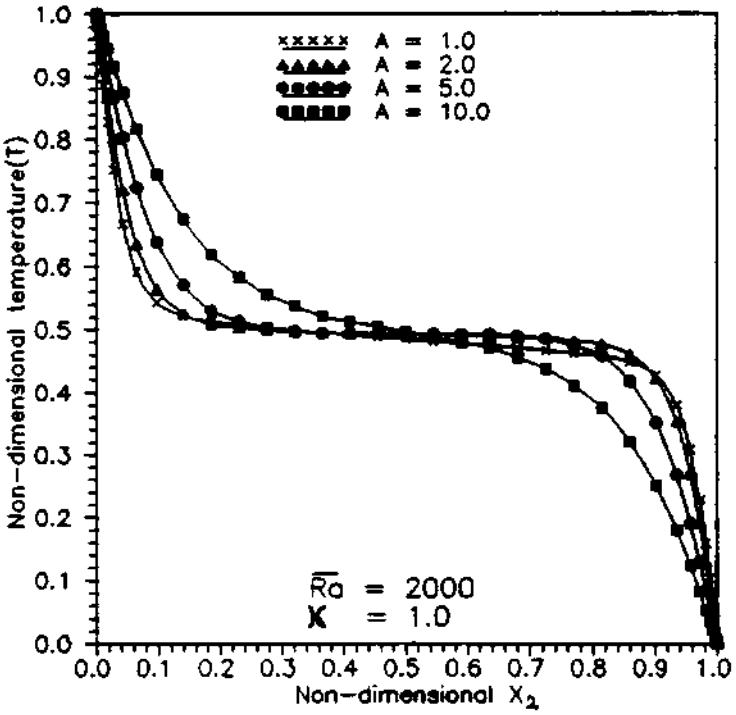

Figure 5.
Variation of temperature along horizontal mid-plane of the annular cavity for different aspect ratios ($\overline{Ra} = 2{,}000$, $\kappa = 1$)

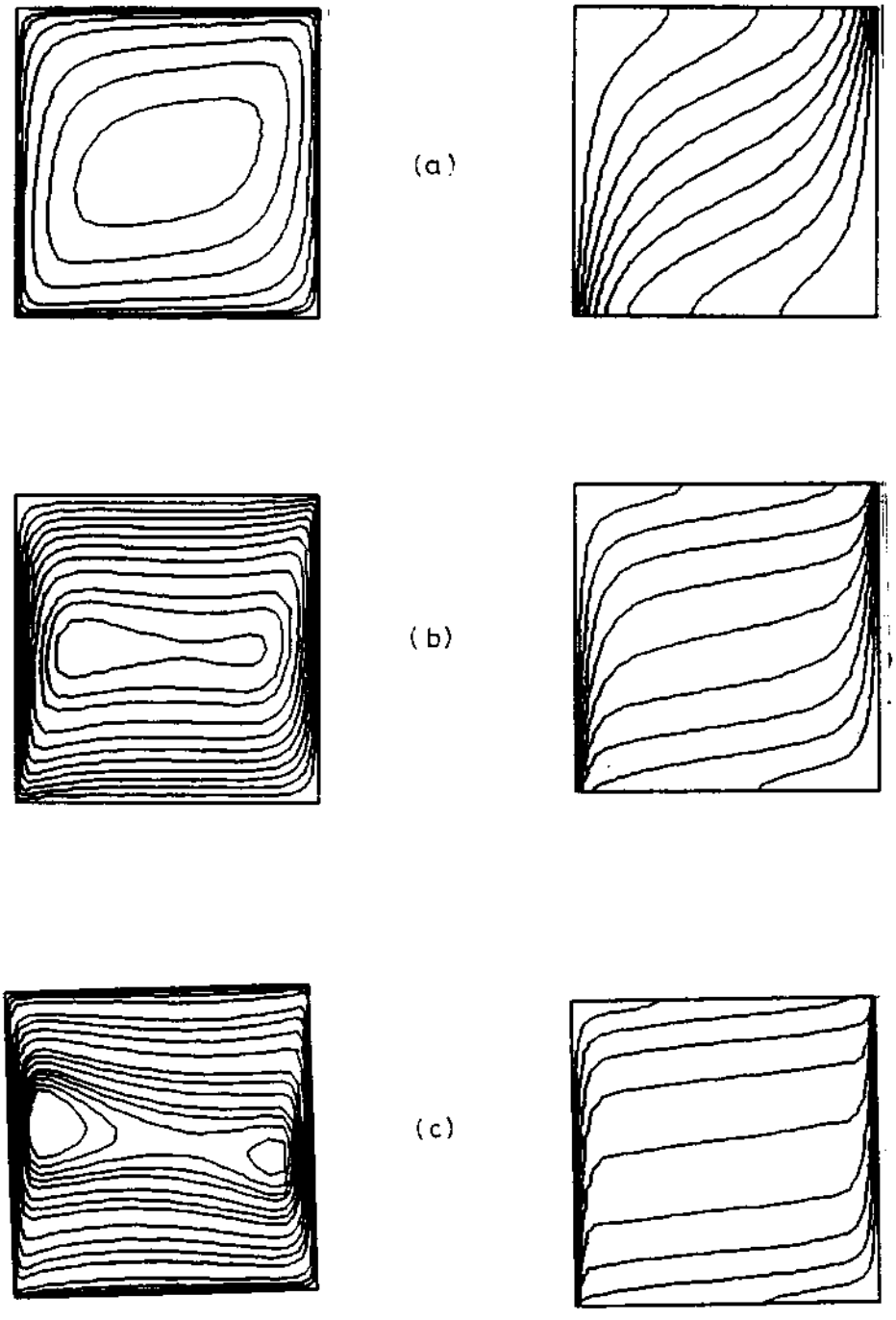

Figure 6.
Streamlines (left) and isotherms (right) for an annular enclosure, $A = 1$, $\kappa = 1$
(a) $\overline{Ra} = 100$,
(b) $\overline{Ra} = 1{,}000$,
(c) $\overline{Ra} = 5{,}000$

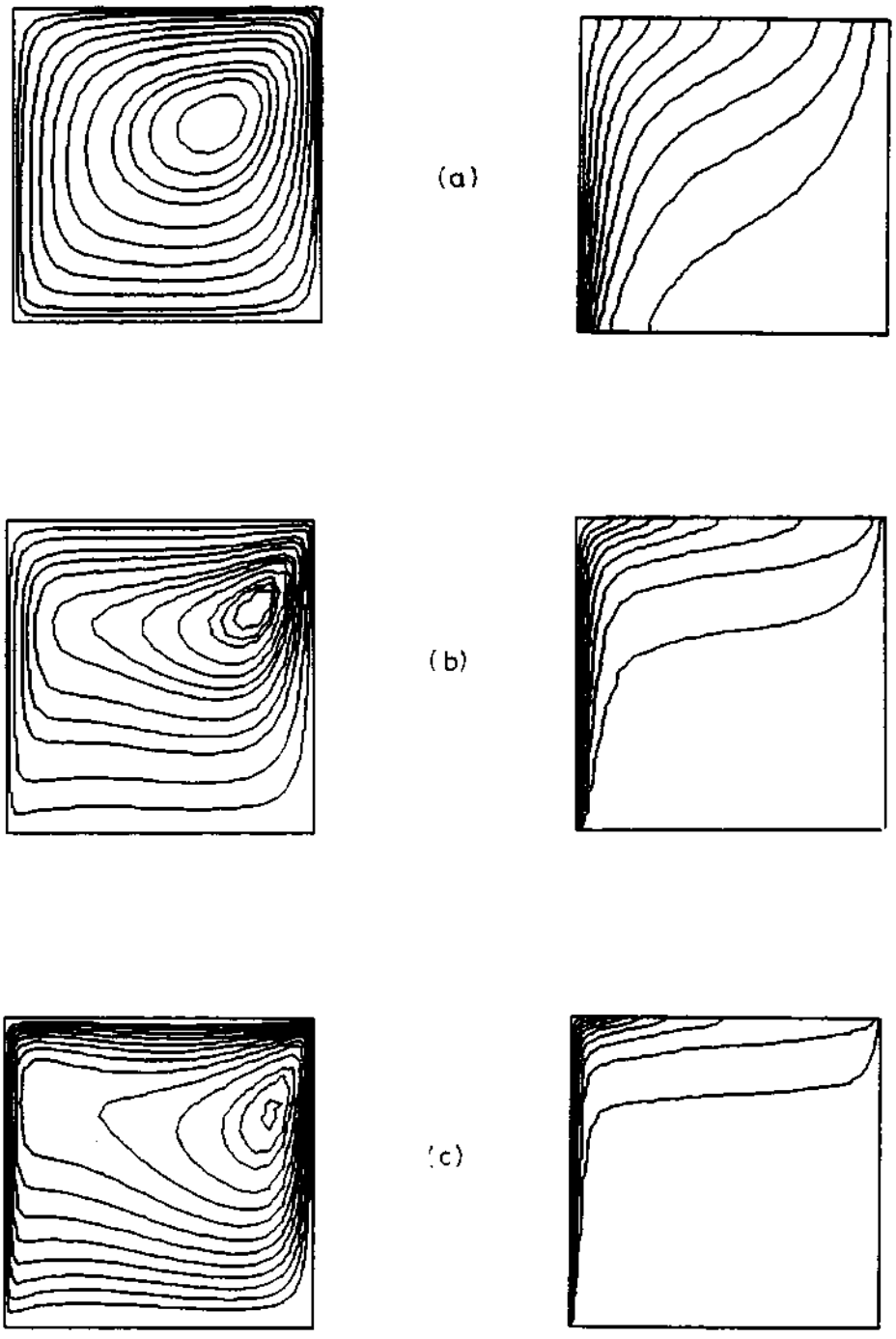

Figure 7.
Streamlines (left) and isotherms (right) for an annular enclosure, $A = 1$, $\kappa = 11$
(a) $Ra = 100$,
(b) $Ra = 1{,}000$,
(c) $Ra = 5{,}000$

the symmetry of isothermal pattern and in turn results in a rapid rise in temperature gradient near the hot wall and, hence, the heat transfer coefficient. The local Nusselt number on the hot wall is given by

$$Nu_i = \left.\frac{\partial T}{\partial X_2}\right|_{X_2=0} \tag{12}$$

Figure 8 shows the influence of radius ratio (κ) on local Nusselt number along the hot wall (Nu_i) for different aspect ratios (A). In general, as κ increases, Nu_i also increases. This is a result of the effect of curvature on the flow and

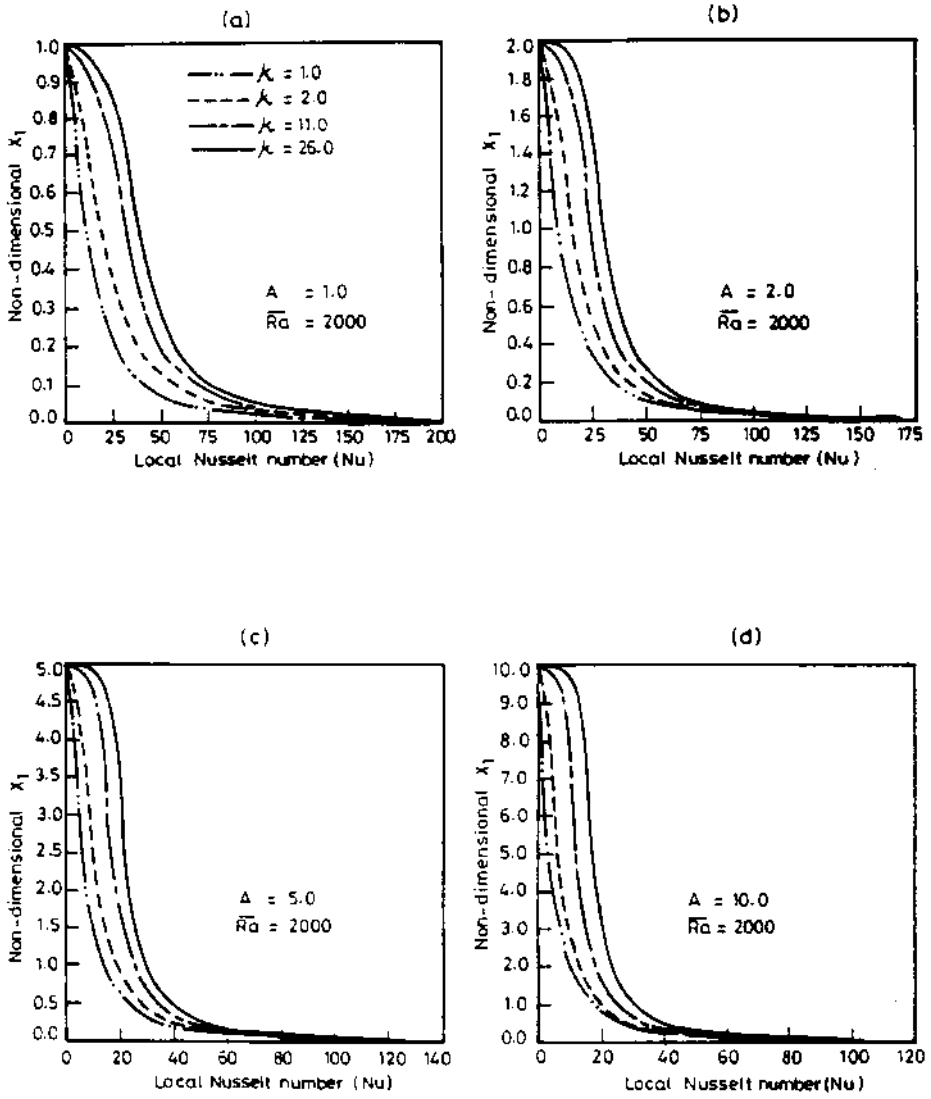

Figure 8.
Variation of local Nusselt number along hot wall of a plane cavity for Ra = 2,000, (a) A = 1, (b) A = 2, (c) A = 5, (d) A = 10

temperature field as discussed earlier. Figure 9 shows the variation of average Nusselt number $\overline{Nu}_i$ along the hot wall with κ for $\overline{Ra}$ = 100, 500 and 2,000 respectively, with A as a parameter. For $\overline{Ra}$ = 100, the slope of $\ln(\overline{Nu}_i)$ versus $\ln(\overline{\kappa})$ curve is almost constant for the whole range of aspect ratios. However, as $\overline{Ra}$ increases, the slope of the curves changes at approximately κ = 2. This effect is more pronounced for A = 1 and at higher $\overline{Ra}$. This result is in contrast with the findings of Prasad and Kulacki[8]. According to [8] the slope changes at κ = 5.

To check the validity of present results, an annular cavity of κ = 5.338 has been considered, for which experimental and numerical results are available [24]. Figure 10 shows $\overline{Nu}_i$ plotted against the modified Rayleigh number $\overline{Ra}$. While the dashed lines show the experimental results of Prasad and Kulocki[24], the dotted lines show their own results obtained numerically using the FDM on the basis of Darcy law. The present results show much better comparison with the experimental results than their own numerical results. A similar comparison with some earlier investigations is shown in Figure 11 for a rectangular cavity of A = 10. The experimental results of Seki *et al.*[25], the boundary-integral solutions of Walker and Homsy[3] and the numerical results of Prasad and Kulacki[8] are plotted along with the present results. Up to $\overline{Ra}$ = 3,000, the present results show much better agreement with the experimental correlation of Seki *et al.*[25] than do the other two. However, at $\overline{Ra}$ > about 3,000, the present predictions are poorer. Based on the results obtained, correlations have been proposed for annular enclosures of aspect ratio 1 and those with aspect ratios ≥ 2. These are:

$$\overline{Nu_i} = 0.369\,\kappa^{0.30}\,\overline{Ra}^{\,0.52}$$

$$\begin{aligned} A &= 1 \\ 1 &\le \kappa \le 26 \\ 100 &\le \overline{Ra} \le 5000 \end{aligned} \tag{13}$$

with a coefficient of correlation 0.991.

$$\overline{Nu_i} = 0.701 A^{-0.40}\,\kappa^{0.32}\,\overline{Ra}^{\,0.43}$$

$$\begin{aligned} 2 &\le A \le 10 \\ 1 &\le \kappa \le 26 \\ 100 &\le \overline{Ra} \le 5000 \end{aligned} \tag{14}$$

with a coefficient of correlation 0.988.

Uniform wall heat flux cases. This subsection of results deals with a rectangular cavity with one of the vertical walls maintained at a uniform heat flux

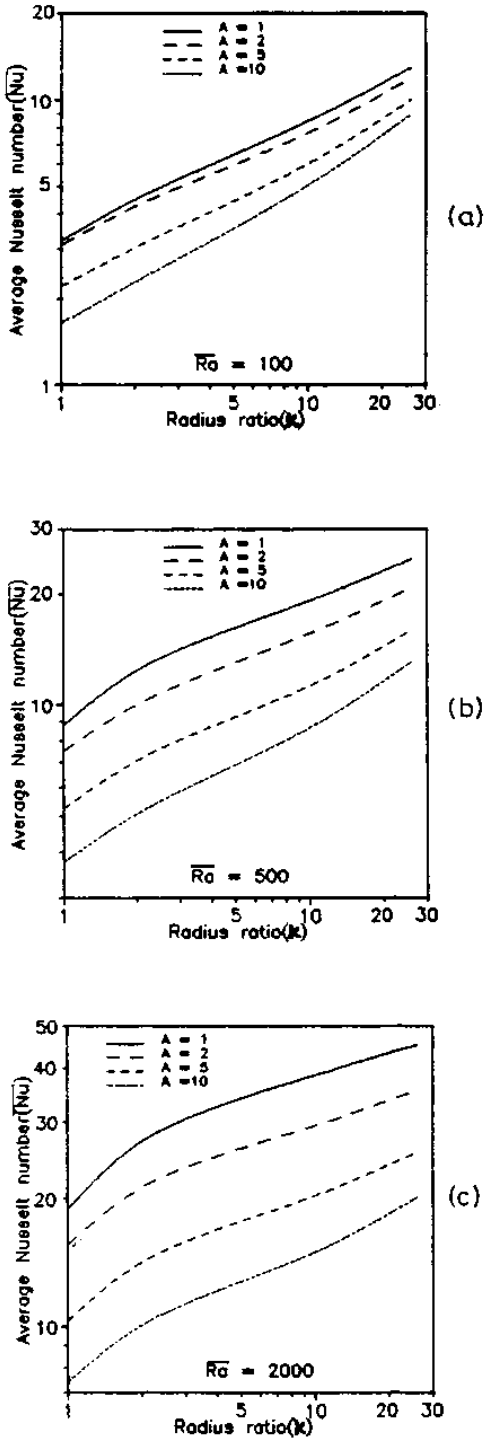

Figure 9.
Variation of $\overline{Nu}_i$ along hot wall of cavity with radius ratio for different aspect ratios
(a) $\overline{Ra}$ = 100,
(b) $\overline{Ra}$ = 500,
(c) $\overline{Ra}$ = 2,000

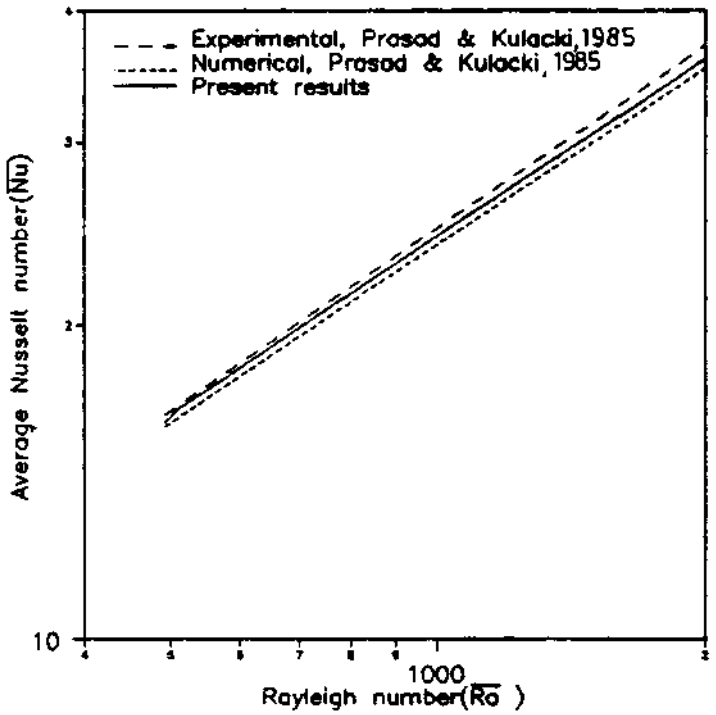

Figure 10.
Comparison of $\overline{Nu}_i$ along hot wall of cavity with experimental results, $k = 5.338$ and $A = 1$

(q), while the other vertical wall loses heat at a uniform temperature ($\overline{T}_0$). This represents a more realistic case of a porous system than the earlier one and finds applications in insulation systems with solar radiation incident on one of the sides. However, as mentioned earlier, the numerical results of [7] were the only ones available in the literature that made use of this type of boundary conditions. Figure 12 shows the geometry and boundary conditions for this problem. Temperature is non-dimensionalized as below:

$$T = \frac{\overline{T} - \overline{T}_o}{\Delta T} \text{ where } \Delta T = \frac{qL_{ref}}{k_m} \tag{15}$$

The range of parameters investigated is given below:

- aspect ratio (A) : 1, 2, 5, 10
- radius ratio (κ) : 1
- Darcy number (Da) : 5×10^{-7}
- modified Rayleigh number Ra^* ($Ra^* = RaDa$) : 100, 200, 500, 1000, 2000, 5000.

Figure 13 shows the non-dimensional temperature (T) along the hot wall of a square cavity for different Ra^*. The slope of the temperature profile is found to be decreasing as Ra^* increases and the temperature profile tends to a uniform

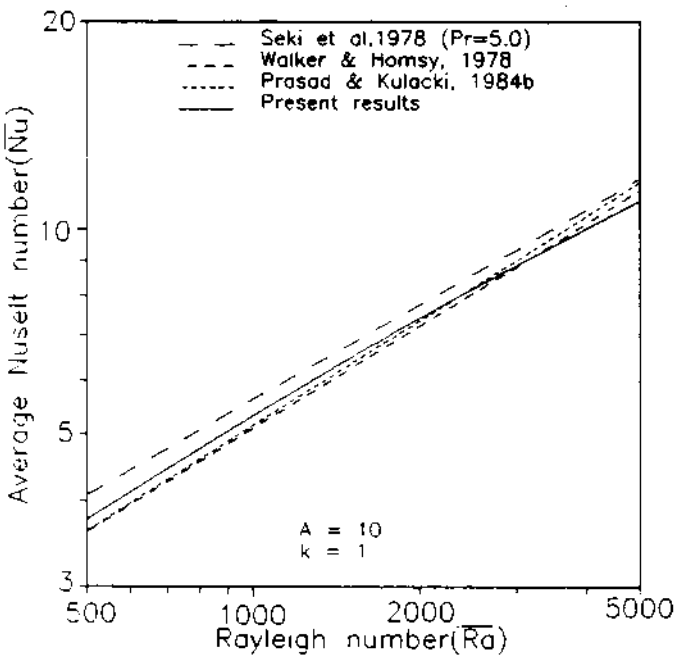

Figure 11.
Comparison of present results with earlier investigations, $A = 10$, $\kappa = 1$

profile at a very high *Ra**. At higher *Ra**, owing to higher strength of convective currents along the hot wall, the temperature becomes more uniform. Figure 14 shows the variation of local Nusselt number (*Nu*) along the hot wall for different *Ra**. *Nu* is calculated as

$$Nu = \frac{AX_1}{T} \tag{16}$$

These trends are in good agreement with those reported in [7]. The effect of aspect ratio (*A*) on temperature and local Nusselt number along the hot wall is brought out in Figures 15 and 16 respectively. Finally, to validate the present results a comparison has been made between the present results and those in Prasad and Kulacki[7] and this is shown in Figure 17. The present results are in excellent agreement with [7]. Similar to the constant wall temperature case, in this section correlations also are proposed over a range of *Ra** from 100 to 5,000 and $A = 1$ and 2 to 10. These correlations are:

$$\overline{Nu} = 0.336 Ra^{*0.40}$$

$$A = 1 \tag{17}$$

$$100 \leq Ra^* \leq 5000$$

with a coefficient of correlation 0.999

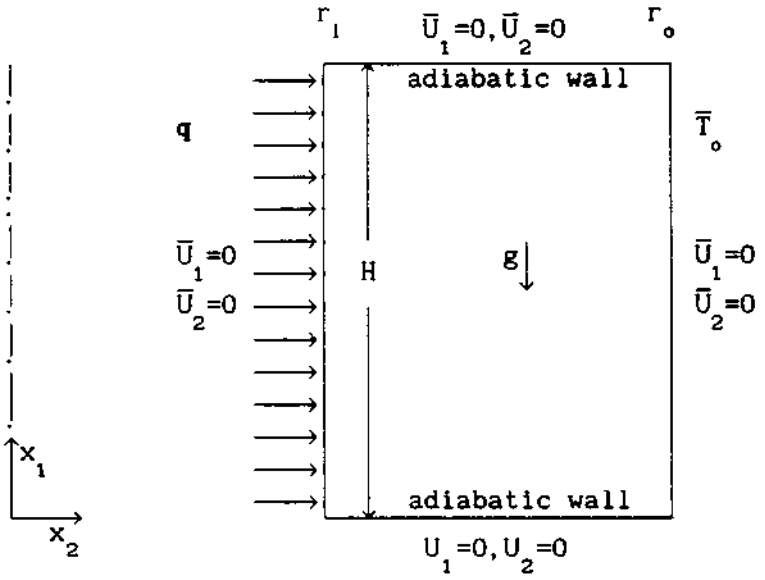

Figure 12.
Geometry and boundary conditions for constant wall heat flux problem

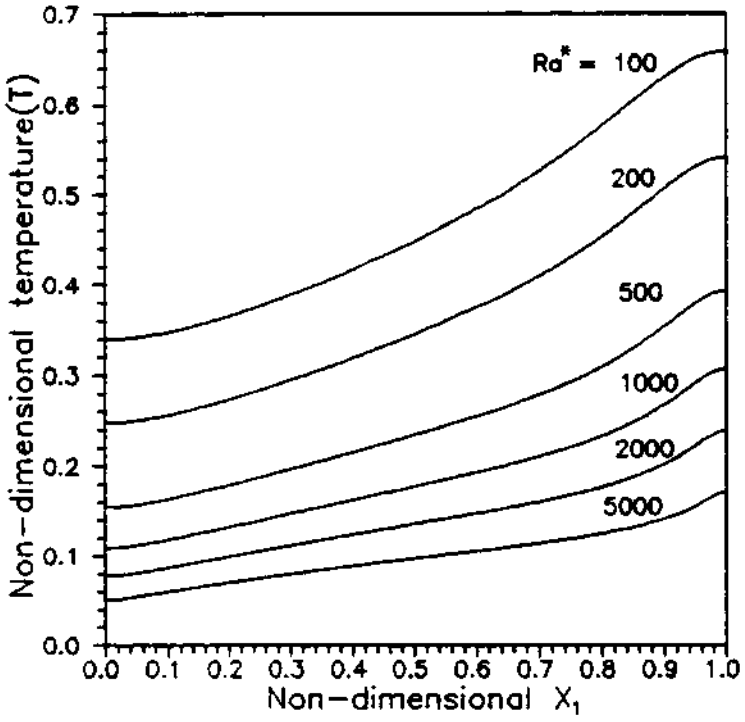

Figure 13.
Variation of temperature along hot wall of a square cavity for different *Ra**

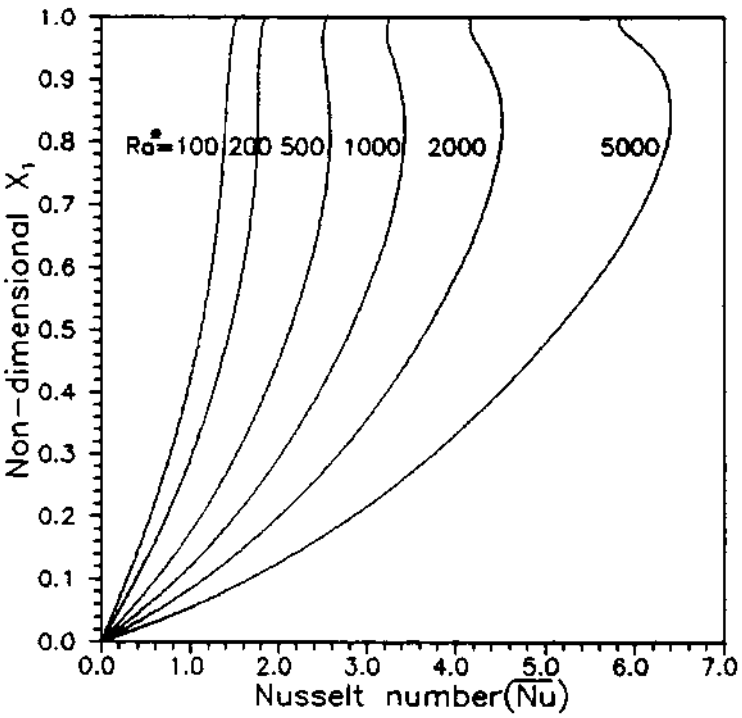

Figure 14.
Variation of *Nu* along hot wall of a square cavity for different *Ra**

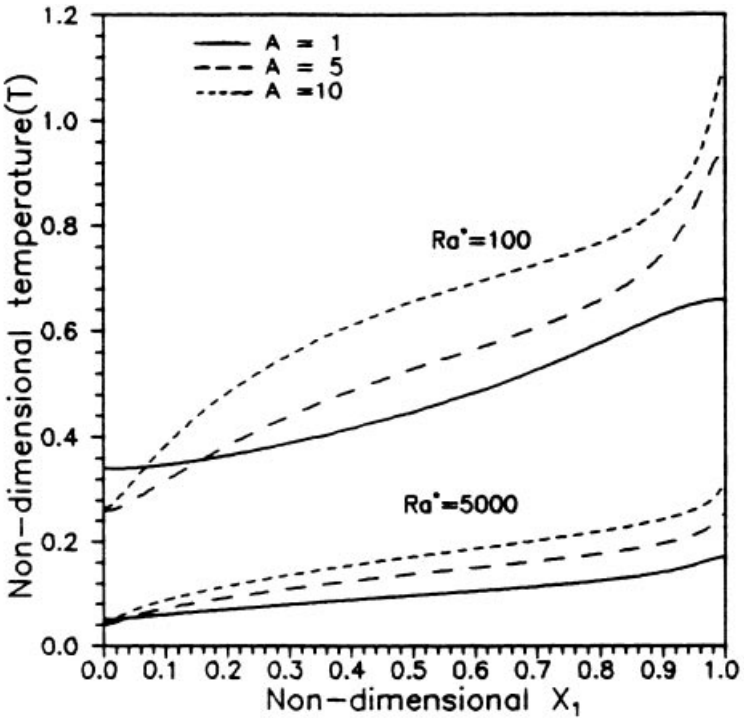

Figure 15.
Effect of aspect ratio on temperature along hot wall of a square cavity

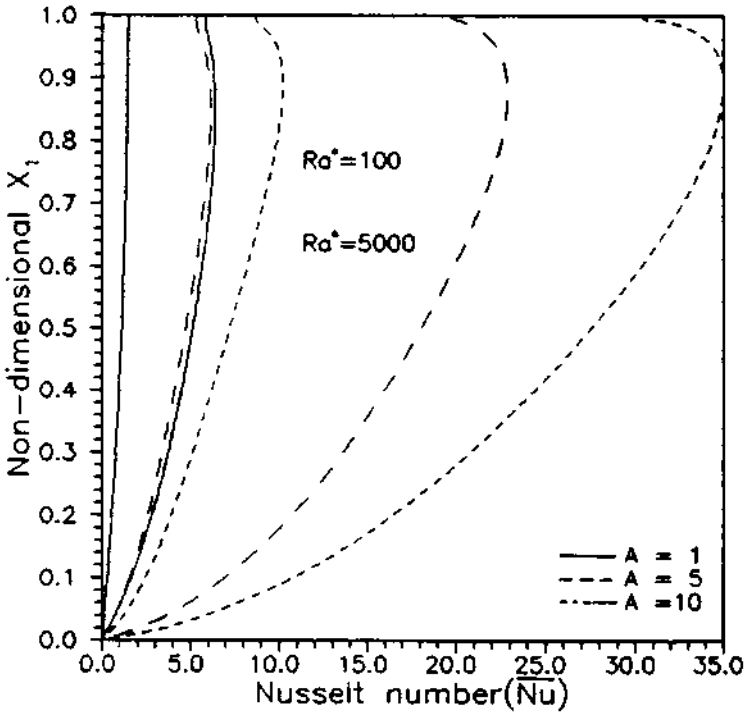

Figure 16.
Effect of aspect ratio on *Nu* along hot wall of a square cavity

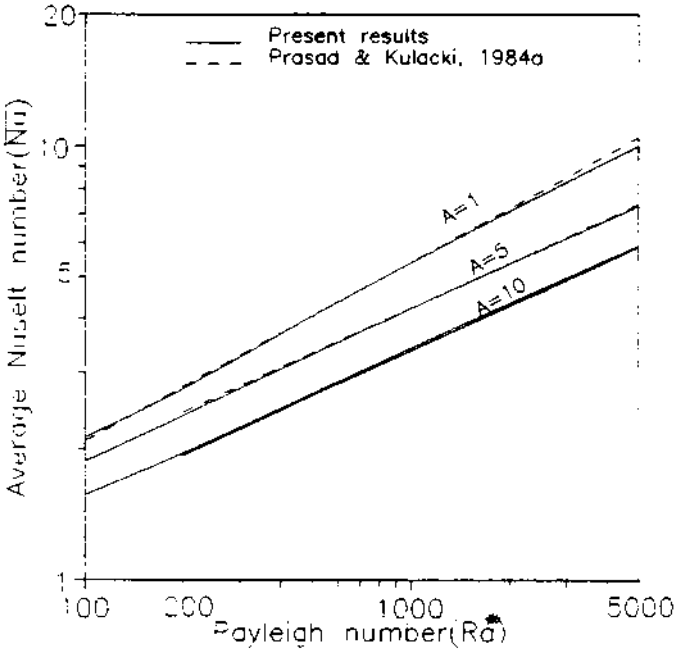

Figure 17.
Comparison of $\overline{Nu}$ of the present study with earlier numerical investigations

$$\overline{Nu} = 0.542A^{-0.25}\,Ra^{*0.35}$$
$$2 \leq A \leq 10$$
$$100 \leq Ra^{*} \leq 5000 \qquad (18)$$

with a coefficient of correlation 0.999.

Investigations in a non-Darcy regime

In this part the present scheme is applied in a high permeability regime where Darcy law becomes questionable. As in the previous section, a non-uniform, graded mesh of size 39×39 nodes with linear triangular elements has been used for all the computations. Two types of boundary conditions considered above are used. However, only rectangular cavities are considered.

Underlying philosophy of present work. In all the previous studies, while providing correlations for $\overline{Nu}$, the combined parameter called modified Rayleigh number $\overline{Ra}$ (or Ra^*) = $RaDa$ has been used. In other words, the significance of Ra and Da has not been brought out separately in the correlations. For example, for a square cavity with side walls subjected to uniform temperatures, $\overline{Nu}$ is of the form

$$\overline{Nu} = (constant)\overline{Ra}^{\,m} \qquad (19)$$

However, alternatively, we could write

$$\overline{Nu} = (constant)Ra^{m}\,Da^{n} \qquad (20)$$

which can be reorganized as

$$\overline{Nu} = (constant)(RaDa)^{m}\,Da^{n-m} \qquad (21)$$

If Darcy law is valid, m would be equal to n and $\overline{Nu}$ would depend solely on $\overline{Ra}$. When a plot is drawn of ln($\overline{Nu}$) versus ln(Da) for a particular Ra, it gives a straight line parallel to the axis on which ln(Da) is taken. However, when permeability is high, it exhibits a straight line behaviour in the region in which Darcy law holds good and changes its slope where the law does not apply. This type of plot was given earlier by Vasseur *et al.*[14] for shallow enclosures and by Lage[17] who used a Brinkman-Forchheimer formulation. The present approach is similar to theirs, but their studies do not suggest any correlations with Ra and Da as separate parameters. In the present work, for the two types of boundary conditions considered, correlations are proposed for a square cavity. Finally, an attempt is also made to bring out qualitatively the effect of aspect ratio (A) on heat transfer coefficient as Da changes.

Uniform wall temperature cases. Figure 1 shows the geometry and boundary conditions employed in this section. Retaining the same notations as before, the range of parameters investigated is as below:

- aspect ratio (A) : 1, 2, 5;
- radius ratio (κ) : 1;
- Darcy number (Da) : 5×10^{-7}, 5×10^{-6}, 5×10^{-5}, 5×10^{-4}, 5×10^{-3}, 5×10^{-2}, 5×10^{-2};
- modified Rayleigh number ($\overline{Ra} = RaDa$) : 10, 50, 100, 500, 1000, 2000, 4000.

The effect of permeability on the velocity field is shown in Figure 18 for $\overline{Ra}$ = 500 and 4,000 respectively. These figures show the vertical velocity profiles along the mid-horizontal plane of a square cavity. For $Da = 5 \times 10^{-7}$, which indicates low permeability, the velocity reaches a peak very near to the hot wall and drops down to almost zero inside the core. This is in conformity with the Darcy law predictions in which a slip is allowed on the wall. As Da increases to 5×10^{-3}, the velocity profile resembles more that in a pure fluid filled cavity. There is a clear boundary layer development. Also, the velocity peak shifts away from the wall and its magnitude decreases. This is so because, for a fixed $\overline{Ra}$, as Da increases, Ra should decrease proportionately. It is Ra which is a measure of buoyancy force, that decides the velocity maximum and, hence, for higher Da, the magnitude of velocity peak is reduced. Also it is observed that for higher Da, somewhere inside the core, the vertical velocity is greater than that for a lower Da. For higher Da, owing to higher viscous forces, the vorticity diffuses through to a greater extent inside the cavity and, hence, a higher velocity is observed inside the core. For $\overline{Ra}$ = 4,000 (Figure 18b), the velocity peaks are much higher than for $\overline{Ra}$ = 500 for the same Da. Also, the boundary layers are much thinner than for $\overline{Ra}$ = 500. This is true as the boundary layers become thinner with increasing buoyancy force.

Similarly, the effect of Da on temperature profiles along the same plane is shown in Figure 19 for $\overline{Ra}$ = 500 and 4,000 respectively. The differences in the temperature profiles as Da changes could be seen more clearly for $\overline{Ra}$ = 4,000 than for 500. It can be inferred that heat diffuses to a lesser extent for lower Da

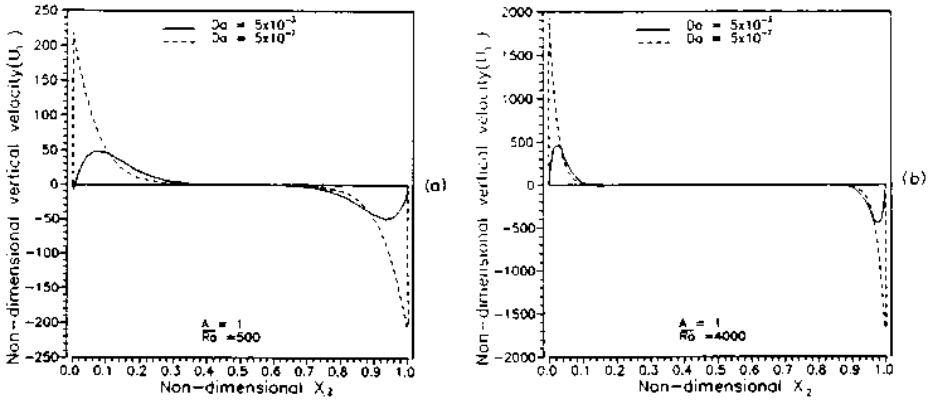

Figure 18.
Variation of non-dimensional vertical velocity along the centre-line of a square cavity with Da as a parameter (a) $\overline{Ra}$ = 500, (b) $\overline{Ra}$ = 4,000

than for higher Da. Also, as Da increases, the temperature profiles start exhibiting inversions (for $\overline{Ra}$ = 4,000). These inversions are responsible for the secondary cells normally observed in cavities filled with pure fluids. Also the temperature profiles do not show significant differences for $Da = 5 \times 10^{-7}$ and 5×10^{-5}. This shows that Darcy law could be safely used for porous medium predictions up to $Da = 5 \times 10^{-5}$.

Figure 20 shows the variation of local Nusselt number along the hot wall of the cavity for $\overline{Ra}$ = 500 and 4,000 with Da as a parameter. Here also, we find that Nu is the same for a large portion of the wall for $Da = 5 \times 10^{-7}$ and 5×10^{-5}. Only near the starting corner, is there a significant difference. The local Nusselt number depends on the thickness of thermal boundary layer. Since, for a fixed $\overline{Ra}$, a lower Da implies a higher Ra, the boundary layer thickness will be smaller for lower Da than for higher Da. Another important observation could be made with regard to Nu for different Das. Even for $Da = 5 \times 10^{-3}$, the local Nusselt number beyond $X_1 = 0.70$ is the same as that for $Da = 5 \times 10^{-7}$. So the effect of permeability is negligible as far as Nu is concerned beyond $X_1 = 0.70$. This is true for both low $\overline{Ra}$ and high $\overline{Ra}$. Figure 21 shows the variation of average Nusselt number ($\overline{Nu}$) with Rayleigh number (Ra), with Da as a parameter. This plot is similar to that obtained by Chan *et al.*[10]. At low Da if one considers a fixed $\overline{Nu}$, Ra increases by the same power as Da decreases and vice versa. This shows the validity of Darcy law. However, as we proceed to the high permeability zone ($Da > 5 \times 10^{-5}$), this relation does not seem to be so simple. This can be better visualized from Figure 22 in which $\overline{Nu}$ is plotted against Da. For different $\overline{Ra}$, the limit of Darcy regime appears to be different, the regime being reduced as $\overline{Ra}$ increases. For $\overline{Ra}$ as low as 10, even at a Da as high as 5×10^{-2}, the Darcy law is valid. But at $\overline{Ra} \geq 500$, this range is limited to less than 5×10^{-5}. Thereafter $\overline{Nu}$ drastically reduces as Da increases. An important feature is that for $\overline{Ra} \geq 500$, even in the non-Darcy regime, the ln($\overline{Nu}$) versus ln(Da) curves show almost linear behaviour.

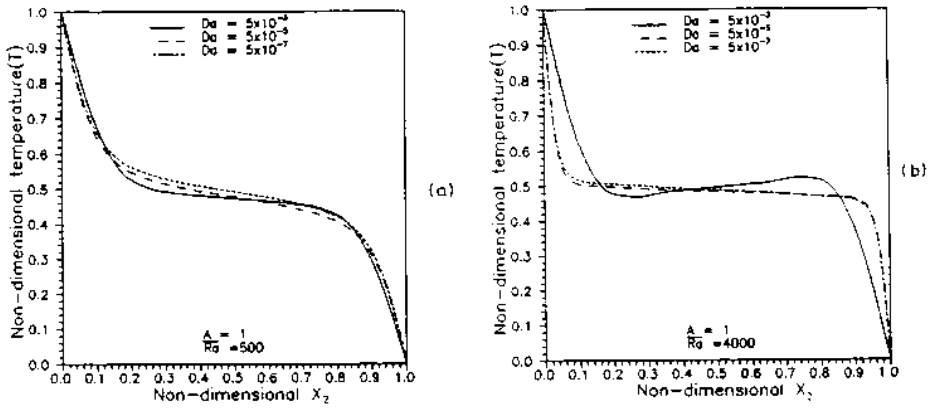

Figure 19.
Variation of non-dimensional temperature along the centre-line of a square vavity with Da as a parameter (a) $\overline{Ra}$ = 500, (b) $\overline{Ra}$ = 4,000

In the literature available so far, no correlations have been proposed for porous media in a non-Darcy regime without combining Ra and Da as a single parameter ($\overline{Ra}$). From Figure 22, it is seen that even though Darcy limits changes for different $\overline{Ra}$, approximately for $\overline{Ra} > 500$ and $Da \geq 5 \times 10^{-5}$ a non-Darcy regime can be assumed to prevail in a square cavity with isothermal side walls. Also within the non-Darcy regime ln($\overline{Nu}$) versus ln(Da) curves are almost linear and hence the relation between $\overline{Nu}$ and Da can be treated by means of a simple power law. Hence, based on the numerical results generated for a square cavity, the following correlation is suggested.

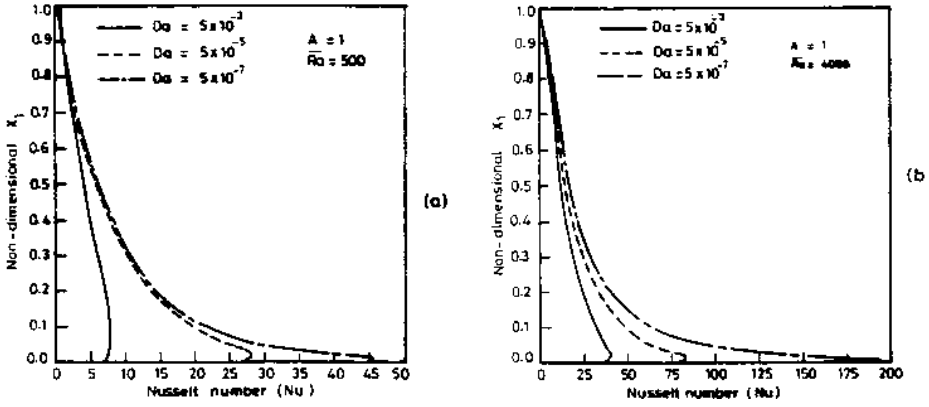

Figure 20.
Variation of local Nusselt number along hot wall of a square cavity with Da as a parameter (a) $\overline{Ra}$ = 500, (b) $\overline{Ra}$ = 4,000

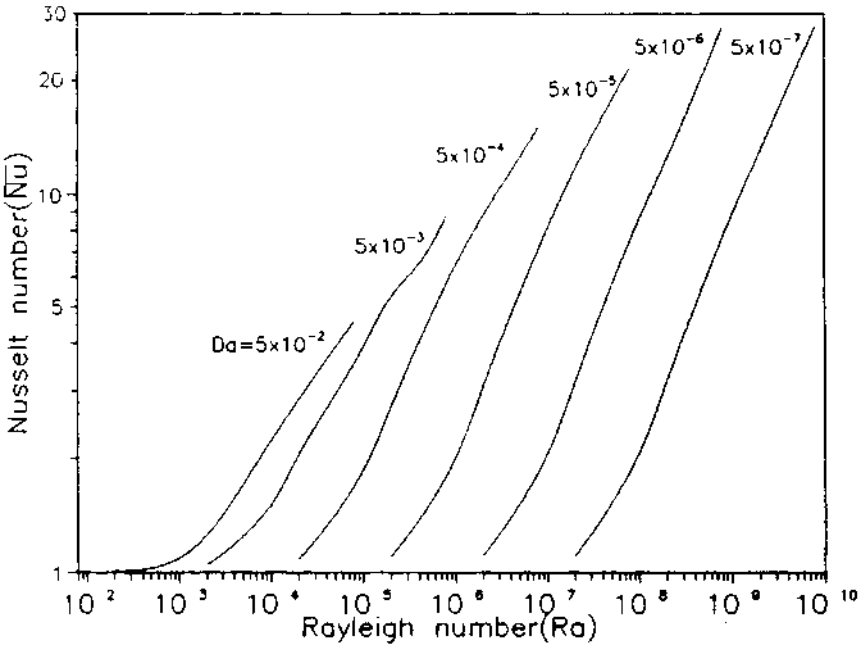

Figure 21.
Variation of average Nusselt number along hot wall of a square cavity for different Rayleigh numbers

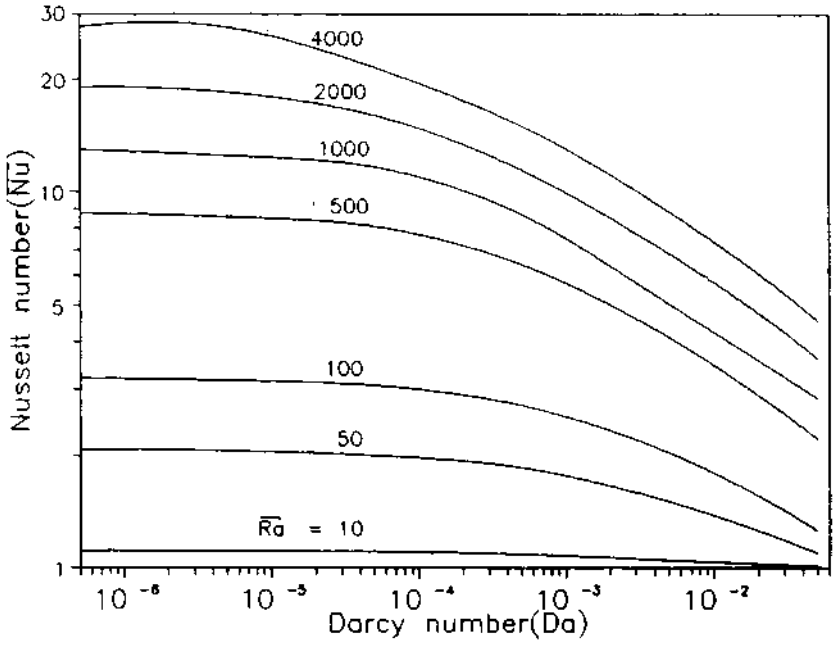

Figure 22.
Average Nusselt number versus Darcy number plots for different $\overline{Ra}$ (aspect ratio = 1)

$$\overline{Nu} = 0.110\, Da^{0.18}\, Ra^{0.39}$$

$$\begin{aligned} \overline{Ra} &\geq 500 \\ Da &\geq 5 \times 10^{-5} \\ A &= 1 \end{aligned} \tag{22}$$

with a coefficient of correlation 0.989. Reorganizing equation (22), we get

$$\overline{Nu} = 0.110\, \overline{Ra}^{0.39}\, Da^{-0.21} \tag{23}$$

Comparing equation (23) with the corresponding correlation above for a Darcy regime, one can infer that in a Darcy regime, $\overline{Nu}$ is independent of Da, while in a non-Darcy regime $\overline{Nu}$ varies inversely as $Da^{0.21}$.

Uniform wall heat flux cases. Figure 12 shows the geometry and boundary conditions for this subsection. The range of parameters investigated are:

- aspect ratio (A) : 1, 5, 10;
- radius ratio (κ) : 1;
- Darcy number (Da) : 5×10^{-7}, 5×10^{-6}, 5×10^{-5}, 5×10^{-3}, 5×10^{-2};
- modified Rayleigh number ($Ra^* = RaDa$) : 10, 100, 1000, 5000.

Figure 23 shows the variation of non-dimensional temperature along the hot wall of a square cavity for Ra^* = 100 and 5,000 for different Darcy numbers. For fixed Ra^* an increase in Da means a decrease in Ra and hence the heat flux on the wall. This, in turn, means a higher non-dimensional temperature on the wall (see equation (15) for temperature non-dimensionalization). Similar to the case of enclosures with constant wall temperatures, here also the effect of Da becomes significant only above $Da = 5 \times 10^{-5}$. Figure 24 shows the local Nusselt number variation along the hot wall of a square cavity for Ra^* = 100 and 5,000. Unlike in the constant wall temperatures case, the local Nusselt number here differs greatly for different Da. It may be recalled that in the former case for $X_1 > 0.70$, there is no significant difference in the Nusselt number distribution for the whole range of Da investigated. On the other hand, in the present case, it is only in the upper half of the cavity height that significant change in the local Nusselt number is seen as Da changes. Once again, one finds a very small difference in the Nusselt number distribution between $Da = 5 \times 10^{-5}$ and 5×10^{-7}. The variation of average Nusselt number $\overline{Nu}$ along the hot wall with Da is plotted in Figure 25 for different Ra^*. Similar observations to those made in the constant wall temperatures case could be made. The non-Darcy regime is reduced as Ra^* increases. The somewhat incomplete curve for Ra^* = 5,000 is due to the fact that difficulties were experienced while obtaining a numerical solution for the case of Ra^* = 5,000 and $Da = 5 \times 10^{-2}$. For the constant wall heat flux case, in the non-Darcy regime the slope of ln($\overline{Nu}$) versus ln(Da) curves is not as marked as it is for the constant wall temperature case. Based on the numerical results for a square cavity, the following correlation is proposed for $\overline{Nu}$:

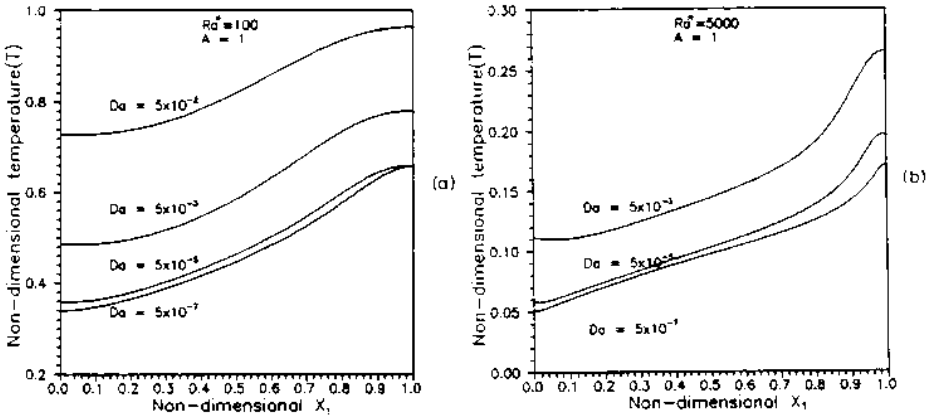

Figure 23.
Variation of non-dimensional temperature along hot wall of a square cavity with Da as a parameter (constant heat flux case) (a) $\overline{Ra}^*$ = 100, (b) $\overline{Ra}^*$ = 5,000

$$\overline{Nu} = 0.191\, Da^{0.33}\, Ra^{0.38}$$

$$Ra^* \geq 100$$

$$Da \geq 5 \times 10^{-5}$$

$$A = 1 \qquad (24)$$

with a coefficient of correlation 0.991. Reorganizing equation (24) we obtain,

$$\overline{Nu} = 0.191\, Ra^{*\,0.38}\, Da^{-0.05} \qquad (25)$$

This shows that the dependence of $\overline{Nu}$ on Da is much weaker for the constant wall heat flux case than for the constant wall temperature case (it may be recalled that the corresponding exponent for the latter is –0.21). This can also be inferred from an examination of Figures 22 and 25 together. The curves in Figure 22 are much steeper in the non-Darcy regime than the curves in Figure 25.

Aspect ratio effects for the two types of boundary conditions. So far all the results presented have been confined to a square cavity (A = 1). In this section, we present a qualitative assessment of the effect of aspect ratio (A) in a non-Darcy regime for both types of boundary conditions considered earlier. The influence of A on the extent of the Darcy regime is shown in Figure 26 for the constant wall temperature case. In this figure $\overline{Nu}$ is plotted against Da for $\overline{Ra}$ = 500 and 2,000 and for A = 1, 2 and 5. While at low Da, the solutions could be obtained even for $\overline{Ra}$ = 4,000, convergence problems are experienced at higher $\overline{Ra}$ and higher Da for A = 2 and 5.

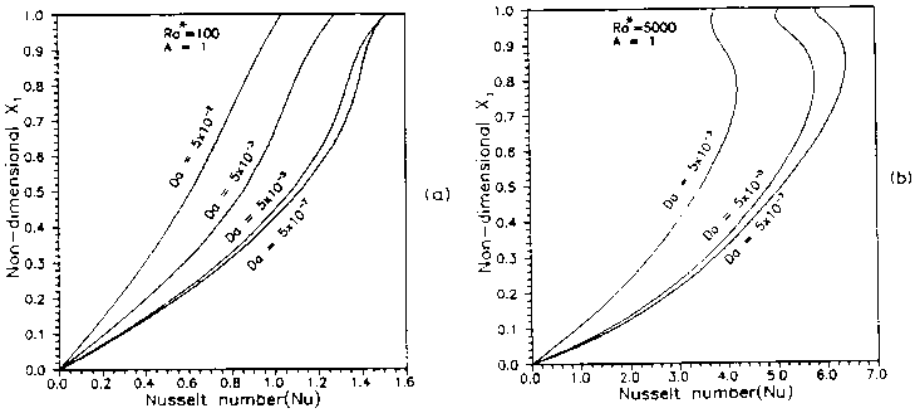

Figure 24.
Variation of local Nusselt number along hot wall of a square cavity with Da as a parameter (constant heat flux case)
(a) $\overline{Ra}^*$ = 100,
(b) $\overline{Ra}^*$ = 5,000

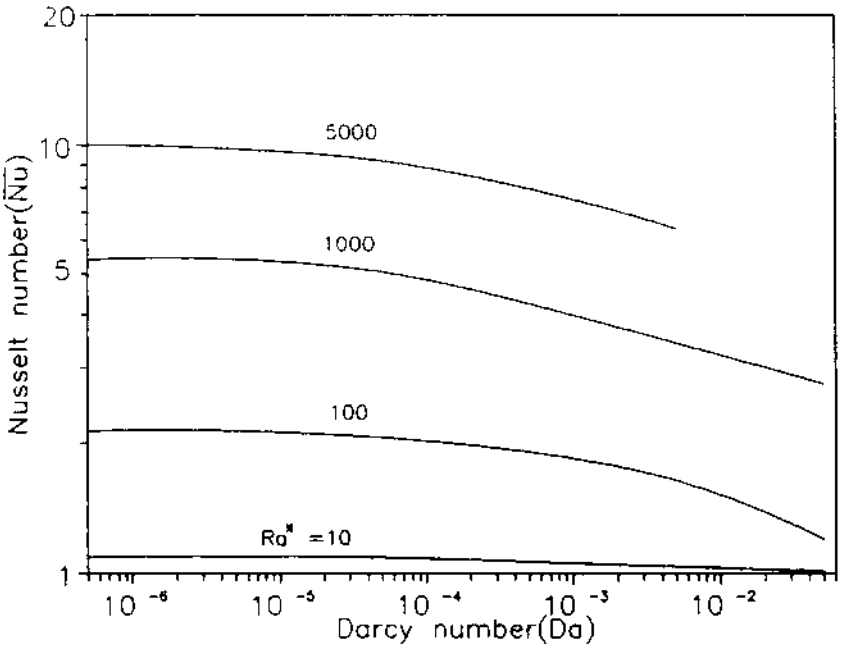

Figure 25.
Average Nusselt number versus Darcy number plots for different *Ra** (aspect ratio = 1)

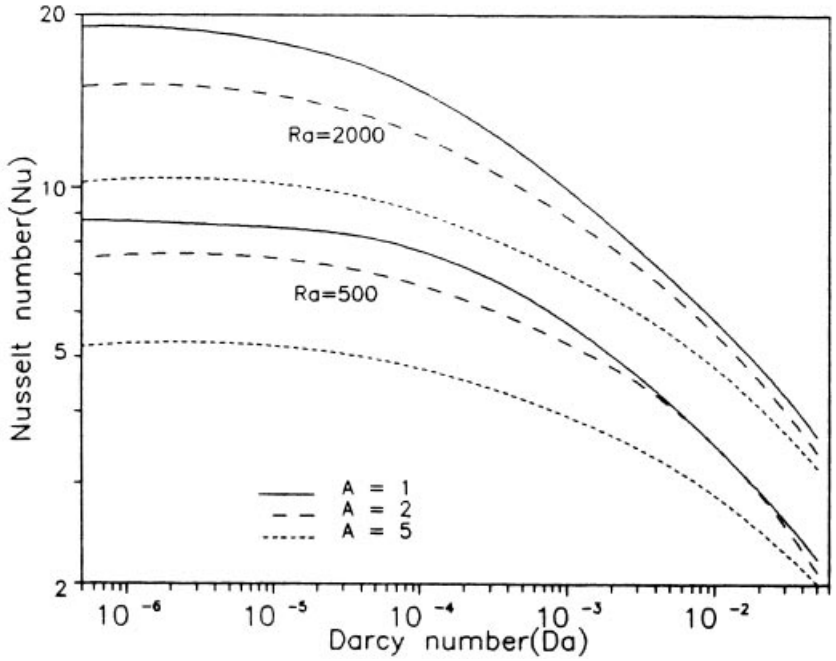

Figure 26.
Effect of aspect ratio on $\overline{Nu}$ versus *Da* plots (constant wall temperatures case)

So the present results are confined to a maximum $\overline{Ra}$ = 2,000 for A = 2 and 5. From this Figure, we observe that aspect ratio significantly affects the non-Darcy behaviour. However, the Darcy number at which the porous medium starts deviating from Darcy behaviour seems to be almost the same for different aspect ratios. But the rate at which $\overline{Nu}$ decreases in a non-Darcy regime is affected by A. For example, considering $\overline{Ra}$ = 500, for A = 1, in a non-Darcy regime, $\overline{Nu}$ drops down much faster than for A = 5. As a result, at some Da, $\overline{Nu}$ for A = 1 even becomes equal to that for A = 5. Similarly for $\overline{Ra}$ = 2,000, $\overline{Nu}$ for A = 1 comes closer to $\overline{Nu}$ for A = 2 and 5 at higher Da. This shows that the dependence of $\overline{Nu}$ on A changes as the permeability changes. At a very low Da of the order of 5×10^{-7}, where Darcy law holds good, $\overline{Nu}$ depends on A as

$$\overline{Nu} \propto A^{-0.40} \tag{26}$$

as given by the correlation proposed above (see equation (14)). The same dependence, according to Prasad and Kulacki[8] is given as

$$\overline{Nu} \propto A^{-0.49} \tag{27}$$

or $\overline{Nu} \propto A^{-0.46}$

depending on whether the radius ratio (κ) < 5 or ≥ 5. However, for pure liquids in enclosures, various experimental investigations (see [26]) suggested that $\overline{Nu}$ varies as $A^{-0.11}$ to $A^{-0.20}$. So as Da increases, the porous medium behaves more like a pure fluid (as has been evidenced from velocity and temperature profiles). Hence the dependence of $\overline{Nu}$ on A becomes weaker. This can clearly be seen in Figure 27 in which $\overline{Nu}$ is plotted against A for $\overline{Ra}$ = 500 and 2,000 with Da as a parameter. Both for $\overline{Ra}$ = 500 and 2,000, as Da decreases, the slopes of $\overline{Nu}$ versus A curves increase. Figures 28 and 29 show corresponding plots for constant wall heat flux case. The curves of A = 1 in Figure 28 drop down much faster than those for A = 5 and 10. Also from Figure 29, which shows $\overline{Nu}$ versus A plots for Ra^* = 100 and 1,000, similar observations as made for the constant wall temperatures case (in Figure 27) can be made. In a low Darcy regime the curves are steeper, which shows that the effect of aspect ratio is significant. For high Da, the plots are almost flat, indicating that the dependence of $\overline{Nu}$ on A is very weak.

Conclusions

The finite element scheme for natural convection heat transfer in porous media developed on the basis of a model that includes both the inertia terms and Brinkman extension has been applied to vertical enclosures in both low permeability (Darcy) and high permeability (non-Darcy) regimes. In Darcy regimes, in the case of annular cavities with constant wall temperatures, the core is observed to be rotating in the streamwise direction. Also, multi-cellular flow pattern has been observed for high $\overline{Ra}$, for an aspect ratio of 1. However, this is seen to die down as radius ratio increases. Also, the multi-cellular flow

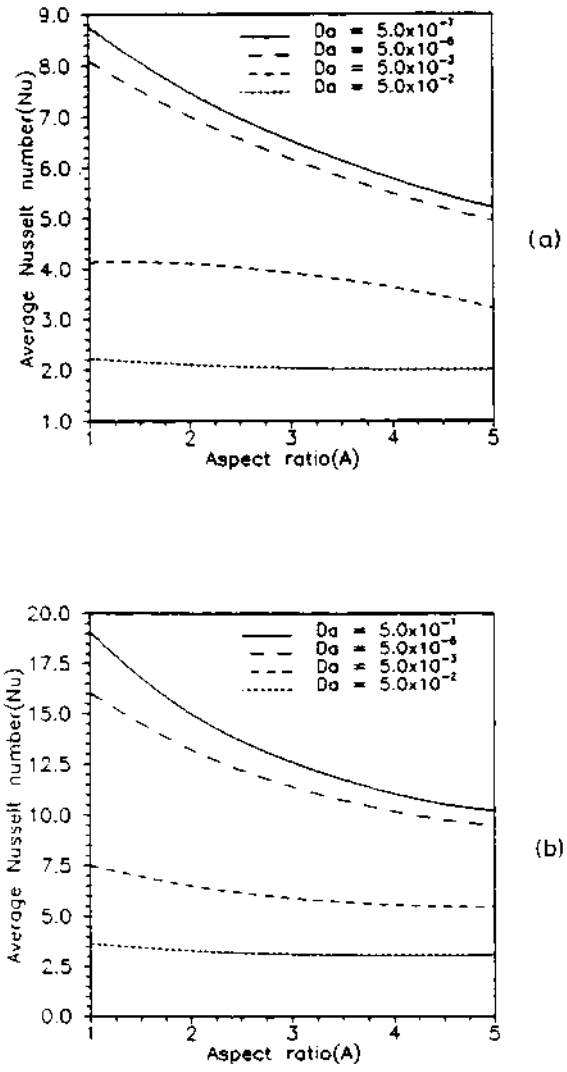

Figure 27.
Average Nusselt number versus aspect ratio plots with *Da* as a parameter (constant wall temperature case) (a) $\overline{Ra}$ = 500, (b) $\overline{Ra}$ = 2,000

pattern is not as strong as in the case of pure fluids. This can be concluded from the fact that the isotherms for porous media do not exhibit a perceptible S-shaped pattern as do the non-porous fluids. The S-shaped profiles are a result of the temperature of the fluid outside the boundary layer being more than that of the fluid at a corresponding point inside the boundary layer. This results in a reversal of the direction of the movement of the fluid particles which, in turn,

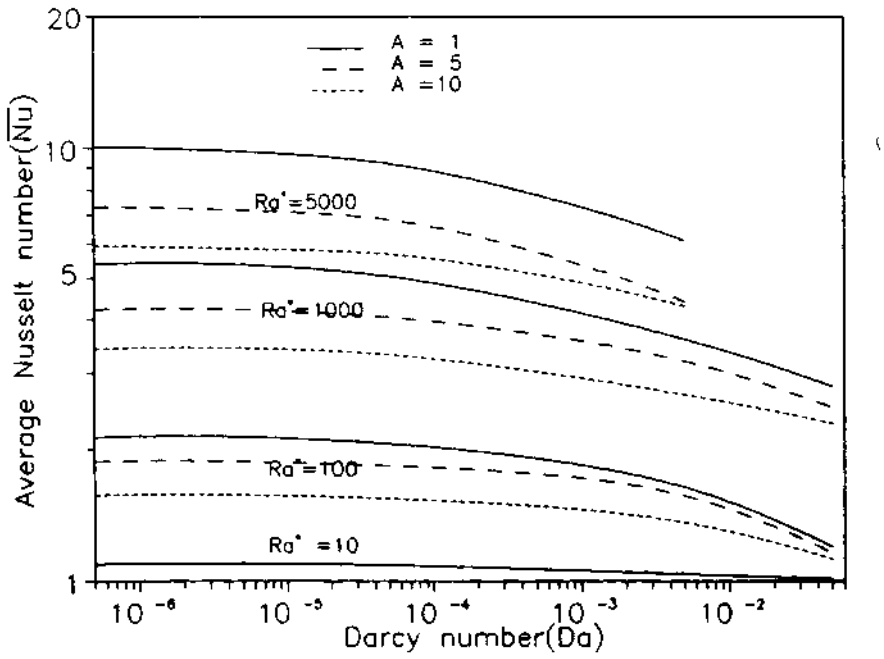

Figure 28.
Effect of aspect ratio on $\overline{Nu}$ versus Da plots (constant wall heat flux case)

leads to cells rotating in the counter direction. In porous media, even though the S-shaped pattern is not conspicuous, at high $\overline{Ra}$ the multi-cellular pattern is seen. New correlations have been presented over a wide range of radius ratios ($1 \leq \kappa \leq 26$) separately for cavities with $A = 1$ and those with $A \geq 2$. These could be used with a fair degree of accuracy over the range of $\overline{Ra}$ and κ investigated. In the case of constant wall heat flux condition, correlations have been proposed for plane cavities with $A = 1$ and those with $A \geq 2$ separately. Equally interesting observations have been made in the non-Darcy regime. Here the velocity field, temperature field and the heat transfer coefficients have been examined in a range of permeability where Darcy law fails to yield accurate results. The phenomenon of the vertical velocity peak shifting away from the wall has been observed as Da increases. Temperature inversions have been observed for higher $\overline{Ra}$ with higher Da. Variations in local Nusselt number have been noticed as Da changes. The effect of permeability on $\overline{Nu}$ has been shown for a square cavity for different $\overline{Ra}$ and Ra^*. Significant differences have been noticed in $\overline{Nu}$ behaviour with Da for the two types of boundary conditions considered. Correlations have been proposed for these two cases without combining Ra and Da as a single parameter. Finally, an attempt has been made to bring out the influence of aspect ratio on heat transfer in rectangular cavity for various permeabilities.

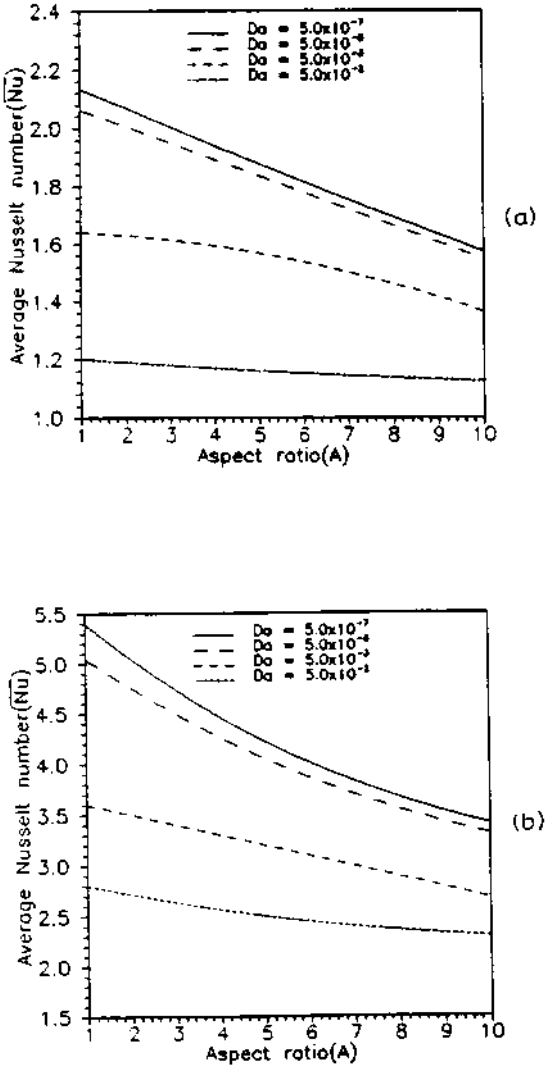

Figure 29.
Average Nusselt number versus aspect ratio plots with *Da* as a parameter (constant wall heat flux case)
(a) $\overline{Ra}^* = 100$,
(b) $\overline{Ra}^* = 1{,}000$

References

1. Weber, J.E., "The boundary layer regime for convection in a vertical porous layer", *International Journal of Heat Mass Transfer*, Vol. 18, 1975, pp. 569-73.
2. Burns, P.J., Chow, L.C. and Tien, C.L., "Convection in a vertical slot filled with porous insulation", *International Journal of Heat Mass Transfer*, Vol. 20, 1977, pp. 919-26.
3. Walker, K.L. and Homsy, G.M., "Convection in a porous cavity", *Journal of Fluid Mechanics*, Vol. 87, 1978, pp. 449-74.
4. Bejan, A., "On the boundary layer regime in a vertical enclosure filled with a porous medium", *Letters in Heat Mass Transfer*, Vol. 6, 1979, pp. 93-102.
5. Simpkins, P.G. and Blythe, P.A., "Convection in a porous layer", *International Journal of Heat Mass Transfer*, Vol. 23, 1980, pp. 881-997.

6. Havstad, M.A. and Burns, P.J., "Convective heat transfer in vertical cylindrical annuli filled with a porous medium", *International Journal of Heat Mass Transfer*, Vol. 25, 1982, pp. 1,755-66.
7. Prasad, V. and Kulacki, F.A., "Natural convection in a rectangular porous cavity with constant heat flux on one vertical wall", *ASME Journal of Heat Transfer*, Vol. 106, 1984, pp. 152-7.
8. Prasad, V. and Kulacki, F.A., "Natural convection in a vertical porous annulus", *International Journal of Heat Mass Transfer*, Vol. 27, 1984, pp. 207-19.
9. Hicox, C.E. and Gartling, D.K., "A numerical study of natural convection in a vertical annular porous layer", *International Journal of Heat Mass Transfer*, Vol. 28, 1985, pp. 720-3.
10. Chan, B.K.C., Ivey, C.M. and Barry, J.M., "Natural convection in enclosed porous media with rectangular boundaries", *ASME Journal of Heat Transfer*, Vol. 2, 1970, pp. 21-7.
11. Tong, T.W. and Subramaniam, E., "A boundary layer analysis for natural convection in vertical porous enclosures – use of the Brinkman-extended Darcy model", *International Journal of Heat Mass Transfer*, Vol. 28, 1985, pp. 563-71.
12. Lauriat, G. and Prasad, V., "Natural convection in a vertical porous cavity: a numerical study for Brinkman-extended Darcy formulation", *ASME Journal of Heat Transfer*, Vol. 109, 1987, pp. 688-96.
13. Sen, A.K., "Natural convection in a shallow porous cavity – the Brinkman model", *International Journal of Heat Mass Transfer*, Vol. 30, 1987, pp. 855-68.
14. Vasseur, P., Wang, C.H. and Sen, M., "The Brinkman model for natural convection in a shallow porous cavity with uniform heat flux", *Numerical Heat Transfer*, Vol. 15, 1989, pp. 221-42.
15. Vasseur, P., Wang, C.H. and Sen, M., "Natural convection in an inclined rectangular porous slot: the Brinkman-extended Darcy model", *ASME Journal of Heat Transfer*, Vol. 112, 1990, pp. 507-11.
16. Joseph, D.D., Nield, D.A. and Papanicolau, G.P., "Non-linear equation governing flow in a saturated porous medium", *Water Resources Research*, Vol. 18, 1982, pp. 1049-52.
17. Lage, J.L., "Effect of convective inertia term on Benard convection in a porous medium", *Numerical Heat Transfer, Part A*, Vol. 22, 1992, pp. 469-85.
18. Vafai, K., Tien, C.L., "Boundary and inertia effects on flow and heat transfer in porous media", *International Journal of Heat Mass Transfer*, Vol. 24, 1981, pp. 195-203.
19. Beji, H. and Gobin, D., "Influence of thermal dispersion on natural convection heat transfer in porous media", *Numerical Heat Transfer, Part A*, Vol. 22, 1992, pp. 487-500.
20. Nield, D.A. and Bejan, A., *Convection in Porous Media*, Springer-Verlag, New York, NY, 1992.
21. Ramaswamy, B., Jue, T.C. and Akin, J.E., "Semi-implicit and expliciti finite element schemes for coupled fluid/thermal problems", *International Journal of Heat Mass Transfer*, Vol. 34, 1992, pp. 675-96.
22. Satya Sai, B.V.K., "Natural convection heat and mass transfer in porous media", PhD Thesis, Indian Institute of Technology, Madras, 1993.
23. Chorin, A.J., "Numerical solution of Navier Stokes equations", *Mathematical Computations*, Vol. 22, 1968, pp. 745-62.
24. Prasad, V. and Kulacki, F.A., "Natural convection in porous media bounded by short concentric vertical cylinders", *ASME Journal of Heat Transfer*, Vol. 107, 1985, pp. 147-54.
25. Seki, N., Fukusako, G. and Inaba, H., "Heat transfer in a confined rectangular cavity packed with porous medium", *International Journal of Heat Mass Transfer*, Vol. 21, 1978, pp. 985-9.
26. Catton, I., "Natural convection in enclosures", *Heat Transfer*, Vol. 6, 1978, pp. 13-43.